Research Square

Preprints are preliminary reports that have not undergone peer review.
They should not be considered conclusive, used to inform clinical practice,
or referenced by the media as validated information.

Tensile Response of Binder-Jetted 316L Stainless Steel to Hydrogen Charging

Emrecan Soylemez

esoylemez@itu.edu.tr

Istanbul Teknik Universitesi https://orcid.org/0000-0003-4827-2606

Cem Örnek

Istanbul Technical University: Istanbul Teknik Universitesi

Burçak Avcı

Istanbul Teknik Üniversitesi: Istanbul Teknik Universitesi

Research Article

Keywords: binder jetting, mechanical strength, hydrogen embrittlement, additive manufacturing

Posted Date: November 27th, 2026

DOI: https://doi.org/10.21203/rs.3.rs-11653306/v1

License: This work is licensed under a Creative Commons Attribution 4.0 International License.
Read Full License

Tensile Response of Binder-Jetted 316L Stainless Steel to Hydrogen Charging

Emrecan Soylemez[1], Cem Örnek[2], Burçak Avcı[2]

Emrecan Soylemez, *esoylemez@itu.edu.tr*, Department of Mechanical Engineering, Istanbul Technical University, Gumussuyu, 34437, Beyoglu, Istanbul, Türkiye
+90 212 2931300/2473, ORCID 0000-0003-4827-2606

Cem Örnek, *cornek@itu.edu.tr*, Department of Metallurgical and Materials Engineering, Istanbul Technical University, Istanbul, Türkiye, ORCID 0000-0002-3029-6493

Burçak Avcı, Department of Metallurgical and Materials Engineering, Istanbul Technical University, Istanbul, Türkiye, ORCID 0000-0002-3595-7852

Abstract

Hydrogen embrittlement limits the use of many steels in hydrogen-exposed applications, and the susceptibility of binder-jetted (BJT) 316L stainless steel to it remains largely unexplored. To test for this susceptibility, miniature tensile specimens were produced by binder jetting and vacuum-sintered at 1370 °C for 90 and 180 min, followed by hydrogen exposure via electrochemical hydrogen charging (50 °C, 7 days) and gaseous hydrogen absorption (20 vol.% H_2 in N_2, 850 °C, 30 min). Vacuum sintering produced a relative density of 98 ± 1%, and doubling the sintering time from 90 to 180 min modestly raised the tensile strength from 380 ± 17 MPa to 400 ± 15 MPa while reducing the ductility from 76 ± 4% to 65 ± 4%. Neither prolonged electrochemical charging nor gaseous hydrogen exposure measurably changed the stress–strain behavior. Scanning electron microscopy fractography confirmed ductile, dimpled fracture in both uncharged and electrochemically charged specimens, with only a few isolated microcracks at void rims in the charged specimen. Binder-jetted SS316L therefore shows practically no hydrogen embrittlement and is a strong candidate for hydrogen-exposed applications.

Keywords: binder jetting, mechanical strength, hydrogen embrittlement, additive manufacturing

1 Introduction

Metal additive manufacturing (AM) offers significant advantages, including weight reduction, part consolidation, rapid prototyping, and enhanced functional performance [1]. As the reliability and mechanical performance of AM components continue to improve, their adoption has become increasingly widespread in aerospace, biomedical, dental, manufacturing, and automotive applications. Consequently, extensive research has been conducted on the mechanical characterization of AM materials [2, 3]. The effects of process parameters and post-processing treatments on static mechanical properties are now relatively well understood for many AM processes and alloys [4–7]. Similarly, low- and high-cycle fatigue behavior, which is critical to the performance of dynamically loaded components, has been extensively investigated in commonly used AM alloys such as Ti-6Al-4V [8], Inconel alloys [9, 10], SS316L [11, 12], and 17-4PH stainless steel [13].

Despite these advances, the performance of AM components under aggressive service environments remains elusive. Properties such as corrosion resistance [14], oxidation resistance [15], wear resistance [6], creep behavior [16, 17], and resistance to hydrogen absorption must satisfy application-specific requirements and industry standards before AM parts can be widely deployed. Among these factors, hydrogen embrittlement has received comparatively limited attention. Among these, hydrogen embrittlement has received comparatively limited attention. The rapid growth of hydrogen-based technologies, including fuel cells, hydrogen storage systems, and high-pressure transportation infrastructure, has increased the need to understand the interaction between hydrogen and AM parts.

Studies so far investigating the hydrogen embrittlement resistance of additively manufactured materials have focused on direct energy deposition (DED) and powder bed fusion using laser beam (PBF-LB) processes. The most frequently examined alloys include SS316L [18], 17-4PH [19] stainless steel, Ti-6Al-4V [20], Inconel 718 [21], Inconel 625 [22], and NiTi shape memory [23] alloys. There is practically no work available on BJT SS316L. 316-grade stainless steel is an important candidate material for hydrogen-related applications due to its low hydrogen absorption and diffusion kinetics and high resistance to hydrogen embrittlement [18, 24–29]. However, hydrogen can still degrade austenitic stainless steels, particularly when the material has high strength, the grain size is large, or the microstructure contains micro-sized secondary phases.

To summarize the current state of knowledge on the mechanical response of AM materials exposed to hydrogen, Table 1 compiles tensile data from selected literature for both material types, tested with and without hydrogen. Hydrogen charging increases tensile strength in most cases and reduces ductility. The ductility loss varies between processing routes and between studies. This scatter calls for a closer look at hydrogen transport in AM and conventional SS316L.

Table 1 Comparison of literature data on the tensile behaviour of conventionally manufactured and additively manufactured molybdenum before and after hydrogen charging. The table summarizes the hydrogen charging procedures, tensile testing strain rates, ultimate tensile strength (UTS), and strain at failure reported in previous studies.

Material	Hydrogen Charging Procedure	Tension Test Strain Rate	UTS (MPa) No H	UTS (MPa) H	Strain at Failure (%) No H	Strain at Failure (%) H	Ref.
Cold Rolled	7 days of 0.1 M NaOH with 3 g/L of ammonium thiocyanate at 80 °C	$10^{-4}s^{-1}$	689	739	85	72	[29]
PBF-LB	7 days of 0.1 M NaOH with 3 g/L of ammonium thiocyanate at 80 °C	$10^{-4}s^{-1}$	577	614	60	58	[29]
PBF-LB Polished	7 days of 0.1 M NaOH with 3 g/L of ammonium thiocyanate at 80 °C	$10^{-4}s^{-1}$	623	653	64	60	[29]
Conventional Wrought	0.1 M aqueous soln. of H_2SO_4 at RT (20 or 115 h)	$1.5 \times 10^{-3}s^{-1}$	572	~565 (20 h) ~580 (115 h)	~55	~60 (20 h) ~57 (115 h)	[25]
PBF-LB	0.1 M aqueous soln. of H_2SO_4 at RT (20 or 115 h)	$1.5 \times 10^{-3}s^{-1}$	674	~665 (20 h) ~640 (115 h)	~50	~40 (20 h) ~38 (115 h)	[25]
DED	75 ◦C for 7 days at 10 mA/cm^2	$10^{-4}s^{-1}$	568	646	37	30	[24]
Conventionally Manufactured	100 MPa H_2 at 270 °C for 400 h	$3.2 \times 10^{-5}s^{-1}$	~640 (RT) ~825 (-50 °C)	~680 (RT) ~790 (-50 °C)			[26]
PBF-LB + HIP	100 MPa H_2 at 270 °C for 400 h	$3.2 \times 10^{-5}s^{-1}$	~605 (RT) ~750 (-50 °C)	~640 (RT) ~785 (-50 °C)			[26]

Previous studies have reported contrasting hydrogen transport and embrittlement behavior in additively manufactured SS316L compared with conventionally manufactured counterparts. While higher hydrogen diffusivity was observed in PBF-LB SS316L at 350–500 °C [18], lower diffusivity was reported at room temperature [29]. Heat treatment at 1066 °C and surface polishing increased hydrogen susceptibility in PBF-LB specimens [29]. Mechanical testing revealed an approximately 20% loss of ductility in PBF-LB SS316L after hydrogen exposure, whereas wrought specimens remained largely unaffected [25]. Similarly, wire-arc-additively manufactured SS316L exhibited increased yield strength and reduced ductility after hydrogen exposure [24]. PBF-LB components tested under hydrogen environments representative of gas regulator service conditions showed a 20% reduction in ductility and a 15% increase in yield strength, with negligible changes in conventionally manufactured counterparts [27]. Despite these concerns, PBF-LB components have demonstrated promising operational stability in proton-exchange-membrane fuel cell applications [28].

Fusion-based AM processes have the potential to produce components suitable for hydrogen-exposed environments. However, to the authors' knowledge, no study has yet investigated the hydrogen embrittlement resistance of binder jetted SS316L parts [30]. In binder jetting, as illustrated in Fig. 1, a powder layer is typically spread by a roller, after which a print head selectively dispenses binder to join powder particles in the regions corresponding to the part geometry [31]. Similar to powder metallurgy and metal injection molding, the printed green part must subsequently undergo post-processing steps, particularly debinding and sintering, to obtain the final consolidated component. Owing to its relatively low machine cost and high production rate, binder jetting

offers an economically attractive alternative to PBF-LB [32]. In this study, SS316L miniature-sized tensile specimens were fabricated and tested for hydrogen embrittlement resistance using electrochemical and gaseous hydrogen charging and post-tensile testing. The effects of refining the sintering recipe on the resulting mechanical response were also examined.

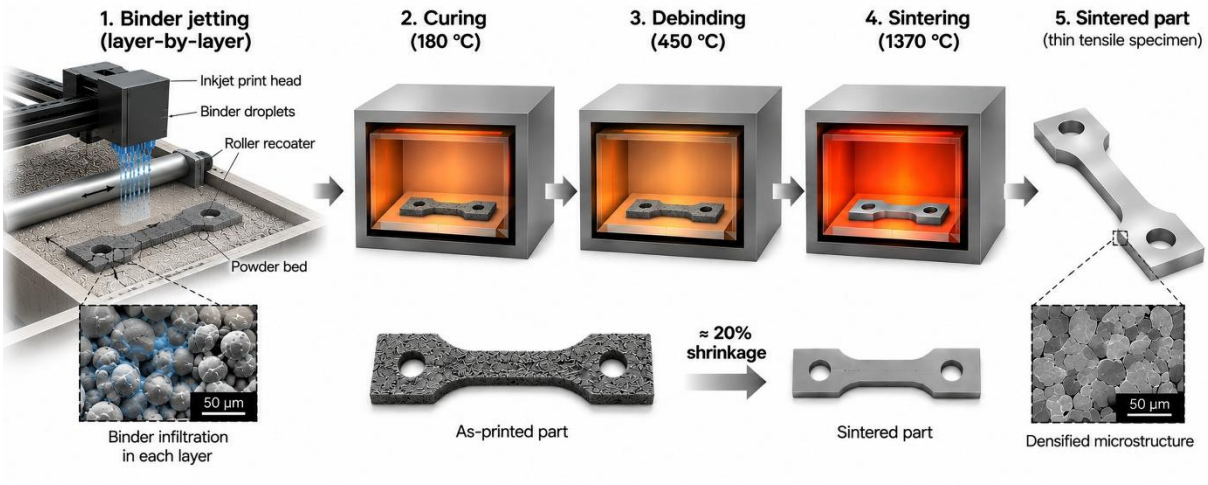


Fig. 1 Schematic illustration of the binder jetting manufacturing workflow, including printing, curing, depowdering, debinding, and sintering stages.

2 Materials and Methods

2.1 Binder jetting

10 × 10 × 10 mm³ cube samples and tensile test specimens with a sintered gauge section of 8 × 3 × 1 mm³ were printed using a Sinterjet M60 BJT machine with a build volume of 65 × 65 × 160 mm³. Powder feeding was performed using a roller, and a solvent-based polymer binder (SR7, Sinterjet) was selectively applied during printing with optimized process parameters can be seen in Table 2. During printing, each layer was dried and partially cured with an infrared lamp, and final curing was performed in an oven at 180 °C for 4 h after printing.

Table 2. Binder jetting process parameters

Process Parameter	Values
Roller translational speed	5 mm/s
Roller rotational speed	40 rpm
Drying time	11 s
Drying power	38 %
Layer thickness	65 µm
Saturation ratio	44 %
Feed ratio	1.7

The particle size distribution was determined by laser diffraction using a Malvern Mastersizer 2000, yielding d_{10}, d_{50}, and d_{90} values of 12, 18, and 27 µm, respectively. The powder density, bulk density, and tap density were 7.88, 3.89, and 4.88 g/cm³, respectively. The Hausner ratio was 1.25, the Hall flow time through a 5 mm orifice was 29.5 s, and the angle of repose was 37.9°. The manufacturer-reported chemical composition (wt.%) was 16.47 Cr, 11.16 Ni, 2.08 Mo, 0.06 Mn, 0.7 Si, 0.01 P, and <0.01 C, with Fe as the balance.

Tap density and bulk density were determined in accordance with ISO 3953 [33] and ISO 3923 [34], respectively, using the Bettersize BeDensi T2 and Bettersize BeDensi B1-S instruments. The powder flow behavior was further

characterized by measuring the Hall flow rate according to BS 5600 [35] using the Bettersize HFLOW-1 device, while the angle of repose was evaluated following ISO 4324 [36].

Samples were printed in four different batches using the same process parameters. In total, 28 cube samples were printed. The average measured dimension was 10.00 ± 0.06 mm in the powder spreading direction (X), 9.94 ± 0.07 mm in the printhead direction (Y), and 10.14 ± 0.08 mm in the build direction (Z). These results indicate good dimensional accuracy and precision in the printed parts. The oversized dimension in the Z direction is attributed to the fact that the 10 mm height is not an exact multiple of the 65 μm layer thickness. The average green density was 50.16 ± 1.06%.

2.2 Debinding and Sintering

Debinding and sintering were carried out in an alumina retort vacuum furnace (KJ-V1700, Kejia Furnace) operated at a base pressure of approximately 7×10^{-2} Pa, following the thermal cycle plotted in Fig. 2. Debinding was conducted at 440 °C for 60–90 min, after which the specimens were sintered at 1370 °C for 90 min or 180 min to achieve high densification while preserving near-end geometry without distortion.

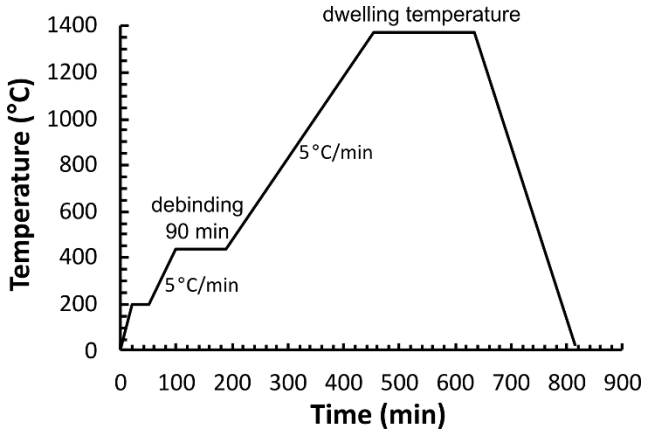


Fig. 2 Thermal schedule for debinding and sintering of binder-jetted SS316L specimens, showing the heating rates, debinding hold, sintering dwell and subsequent cooling.

The cube specimens were measured after printing and sintering with a caliper to 0.01 mm resolution, and each dimension was recorded based on three consecutive measurements. Each specimen was weighed using a precision balance with a sensitivity of 0.1 mg. The green density was then calculated by dividing the measured mass by the corresponding specimen volume. For the sintered specimens, relative density was additionally determined using the Archimedes' method [37], and the reported density values for the sintered condition are based on these measurements.

The sintered cube samples reached an average relative density of 94.82%, with a standard deviation of 1.31%. The average anisotropic shrinkage values were 19.98%, 20.31%, and 20.41% in the X, Y, and Z directions, respectively. The tensile specimens were fabricated with a density of 97.98 ± 0.84%.

2.3 Tensile testing and hydrogen exposure

Tensile tests were performed on as-built dogbone specimens with a 5 kN Deben micro-tensile tester at a crosshead speed of 0.1 mm/min corresponding to a strain rate of 2 × 10–4 s–1. The specimen is shown in Fig. 3 with

photographs of the as-printed (green) and sintered specimens. Force and elongation were recorded at 500 ms intervals. Engineering strain was calculated as the crosshead displacement divided by the 8 mm gauge length, and stress was calculated as the force divided by the nominal area. Each condition was tested in triplicate, and the average stress–strain curve was calculated and plotted with ± one standard deviation. Gaseous hydrogen-charged specimens were tested in duplicate. Following tensile testing, the fractured specimens were cold-mounted with the broad face exposed, wet-ground, and polished to a 1 µm diamond finish to examine microstructural performance under deformation. The microstructure was revealed by etching in 10 wt.% oxalic acid for 2 min at room temperature and examined using a Hirox digital microscope.

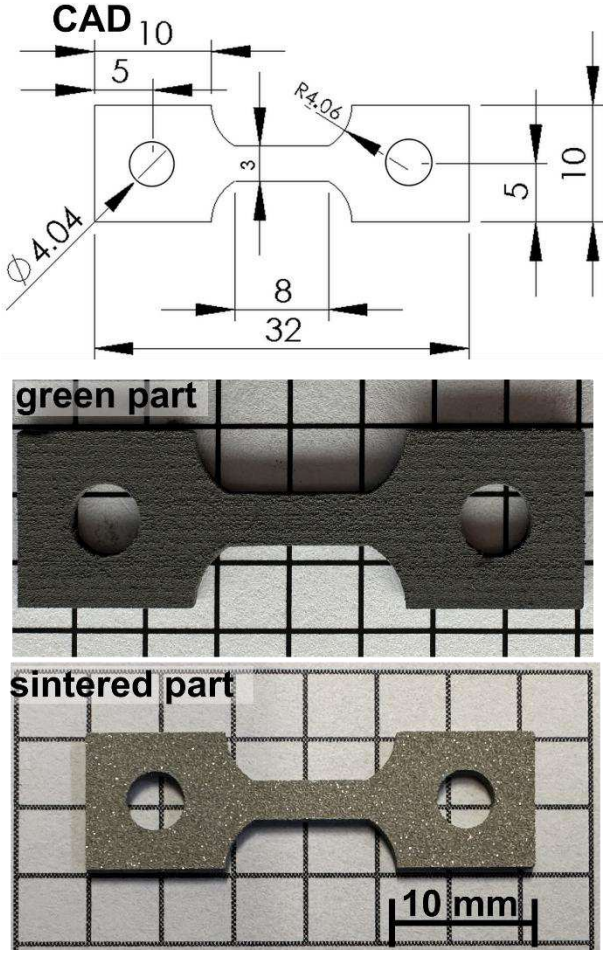


Fig. 3 Technical drawing of the miniature tensile specimen (dimensions in mm) and photographs of representative as-printed green and sintered specimens. The photographs are scaled to their real relative sizes, showing how the green part shrinks to its actual size after sintering.

Selected specimens were subjected to two distinct hydrogen exposure methods: (i) electrochemical charging and (ii) high-temperature gaseous hydrogen exposure. Electrochemical charging was performed in 0.1 M NaCl at 50 °C under galvanostatic cathodic polarisation at −10 mA/cm² for one week, using a two-electrode cell with a platinum counter electrode. These conditions represent the upper operating limits of the electrochemical charging setup. The hydrogen penetration depth was estimated using the temperature-dependent hydrogen diffusivity, described by the Arrhenius relation:

$$D = D_0 \exp(-E_a/RT) \quad (1)$$

where D_0 = (7.3 ± 0.9) × 10−7 m²/s is the pre-exponential factor, E_a = 52.4 kJ mol^{-1} is the activation energy [38], R is the gas constant, and T is the absolute temperature. The penetration depth x after a charging time t was estimated as

$$x = 2\sqrt{Dt} \tag{2}$$

At 50 °C, D is 2.5 × 10^{-15} m²/s, and one week of charging gives a penetration depth of about 77 µm in Fig. 4b. At 850 °C, D is 2.7 × 10^{-9} m²/s, and 30 min gives about 4.4 mm. This exceeds the specimen half-thickness of ~0.5 mm. Gaseous charging at 850 °C was therefore used to charge the full cross-section. Two additional specimens were hydrogenated from the gas phase in a flow-through tube furnace. The furnace was flushed with H_2 at 40 ml/min and N_2 at 160 ml/min (20 vol.% H_2). It was heated at 4 °C/min to 850 °C and held for 30 min. The furnace was then switched off, and the specimens cooled to room temperature inside it. The H_2–N_2 flow was maintained down to 150 °C. Below 150 °C, only N_2 was purged. Tensile tests were typically performed within 1 h after the end of hydrogen charging.

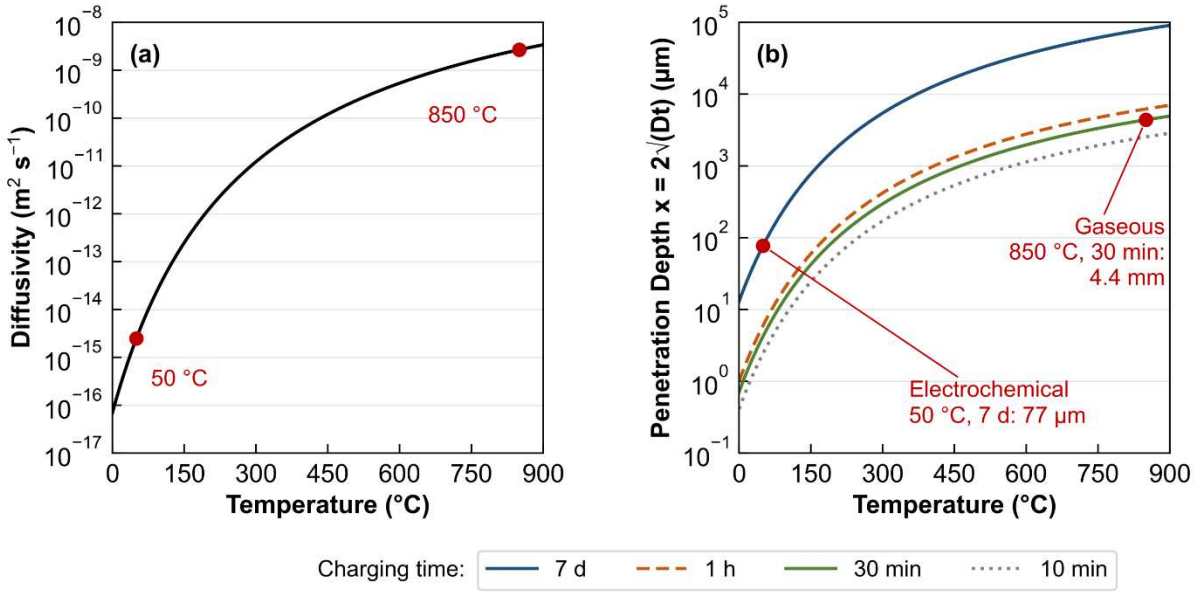


Fig. 4 Hydrogen diffusivity and penetration depth as a function of temperature. (a) Diffusion coefficient $D = D_0\, exp(-E_a/RT)$ with D_0 = (7.3 ± 0.9) × 10^{-7} m²/s and E_a = 52.4 kJ/mol. (b) Penetration depth $x = 2\sqrt{(Dt)}$ for charging times of 10 min, 30 min, 1 h and 7 d. The red markers show the electrochemical (50 °C, 7 d) and gaseous (850 °C, 30 min) charging conditions.

The fracture surfaces of the tensile specimens were analyzed using a Zeiss EVO 10 scanning electron microscope (SEM). Images were acquired with the backscattered electron (BSE) detector.

3 Results

Microstructure—The microstructure consists of equiaxed grains of 100–150 µm in size with annealing twins (Fig. 5). Rounded dark features were distributed throughout the microstructure, representing residual pores from sintering and cavities left by inclusions dislodged during polishing. Following exposure to gaseous hydrogen, the grain morphology, annealing twins, and cavity distribution remained comparable to those of the uncharged specimen. No obvious differences between the two conditions were observed by optical microscopy.

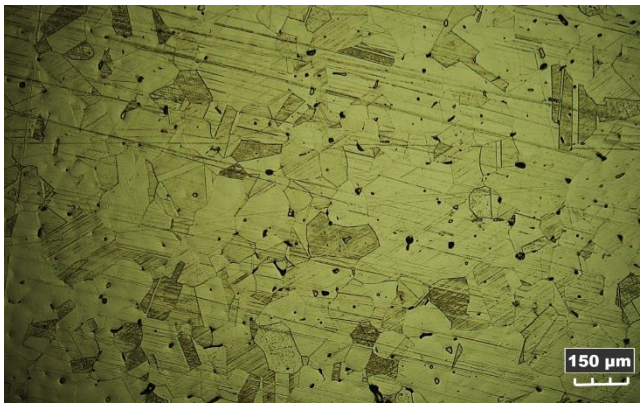


Fig. 5 Microstructure of a binder-jetted tensile specimen showing equiaxed grains and twin boundaries in line with a conventionally fabricated austenitic stainless steel. The microstructure was revealed with oxalic acid etching.

Stress–Strain behavior—Specimens debound for 60 min exhibited lower ultimate tensile strength (348 ± 23 MPa) and strain at failure (52 ± 3%) than those debound for 90 min. Figure 6 compares the stress–strain responses of specimens debound for 90 min and sintered at 1370 °C for 90 and 180 min, with the corresponding tensile properties summarized in Table 3.

Extending sintering from 90 to 180 min improved tensile strength but reduced ductility. Property variations may partly reflect fluctuations in furnace temperature (±5 °C) and spatial gradients. Figure 6 also compares the tensile responses of uncharged, electrochemically hydrogen-charged (EHC) and gaseous hydrogen-charged (GHC) specimens, with corresponding properties summarized in Table 3 (n = 3 per condition, except GHC, n = 2). Yield strengths remained near 120 MPa, and neither charging method caused premature failure or reduced ductility beyond the scatter observed in uncharged specimens. GHC specimens exhibited the highest strain at failure, although the difference was within experimental variability.

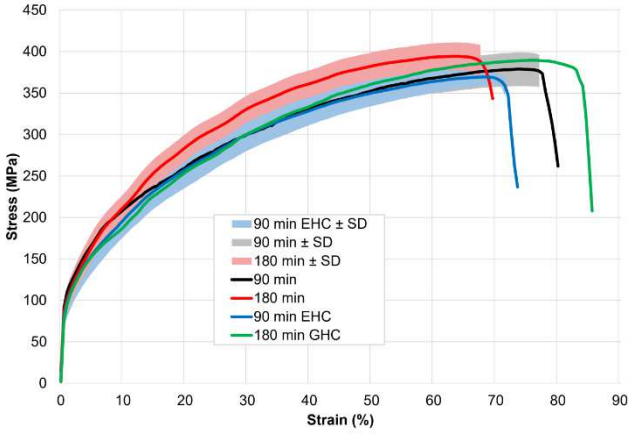


Fig. 6 Stress–strain curves of specimens debound for 90 min and sintered at 1370 °C. Curves show uncharged specimens sintered for 90 min (black) and 180 min (red), electrochemically hydrogen-charged (EHC) specimens sintered for 90 min (blue), and gaseous hydrogen-charged (GHC) specimens sintered for 180 min (green). Shaded bands indicate ± one standard deviation.

Table 3. Tensile properties of uncharged and hydrogen-charged specimens debound for 90 min and sintered at 1370 °C.

Sintering Time	UTS (MPA) No H	UTS (MPA) EHC	UTS (MPA) GHC	ε at Failure (%) No H	ε at Failure (%) EHC	ε at Failure (%) GHC
90 min	380 ± 17	370±10	400±10	76±4	71±5	82±7
180 min	400 ± 15	410±10	390	65±4	66±1	85

After tensile loading to fracture, the grains of the uncharged specimen contain dense slip bands, and the cavities are elongated along the loading axis (Fig 7a). Next to the fracture surface, the cavities are larger and more clustered (Fig 7b).

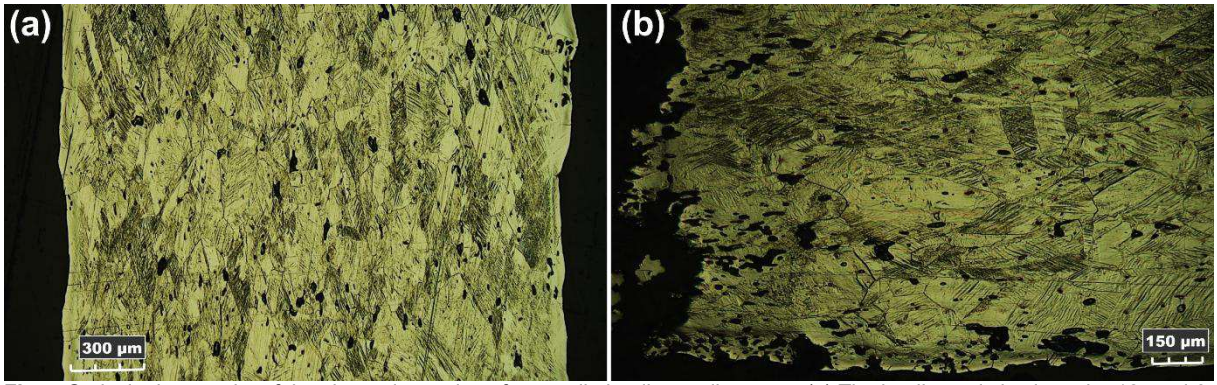


Fig. 7 Optical micrographs of the sintered samples after tensile loading until rupture. (a) The loading axis is along the 12- and 6-o'clock directions. The grains contain dense slip bands, and the cavities are elongated along the loading axis. (b) Region next to the fracture surface after tensile loading until rupture. The loading axis is along the 3- and 9-o'clock directions. The cavities are elongated along the loading axis. Near the fracture surface, voids nucleated at these features grew and coalesced during necking.

After gaseous hydrogen charging, the grain structure, the annealing twins and the distribution of cavities remain unchanged. The gaseous-hydrogen-charged specimen exhibits the same deformation features after fracture. The grains contain dense slip bands, and the cavities are elongated along the loading axis (Fig. 8a). The gauge section narrows toward the fracture, and the fracture surface is inclined to the loading axis (Fig. 8b). Larger cavities formed by linked voids appear near the specimen edges.

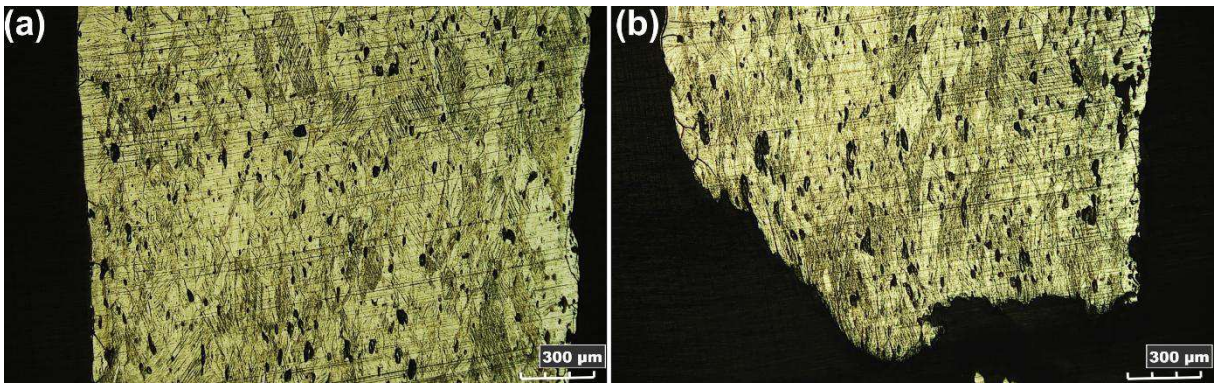


Fig. 8 Optical micrographs of the as-built AM microstructure after gaseous hydrogen charging (20 vol.% H_2 in N_2, 850 °C, 30 min), shown on the broad face of the dogbone specimen, showing the microstructure (a) after tensile loading until rupture. The grains contain dense slip bands. (b) Fractured end of the gauge section. The gauge section narrows toward the fracture, and the fracture surface is inclined to the loading axis on the left. Larger cavities formed by linked voids appear near the specimen edges.

Fractography—Figure 9 and Figure 10 show SEM images of the fracture surfaces of an uncharged and an electrochemically hydrogen-charged specimen, respectively. Both surfaces are covered by dimples of different sizes, and the specimen edges are rough where the material tore (Fig. 9a, Fig. 10a). At higher magnification, the dimples are smooth-walled and cup-shaped, separated by sharp ridges, and some contain residual particles (Fig. 9b-c). The charged specimen shows the same dimple morphology in both framed regions (Fig. 10b-c). Neither condition shows extended flat or faceted regions. The only difference is that tiny cracks were found at a few isolated sites on the charged specimen, at the rim of microvoids shown with the green frame and arrow in Fig. 10b.

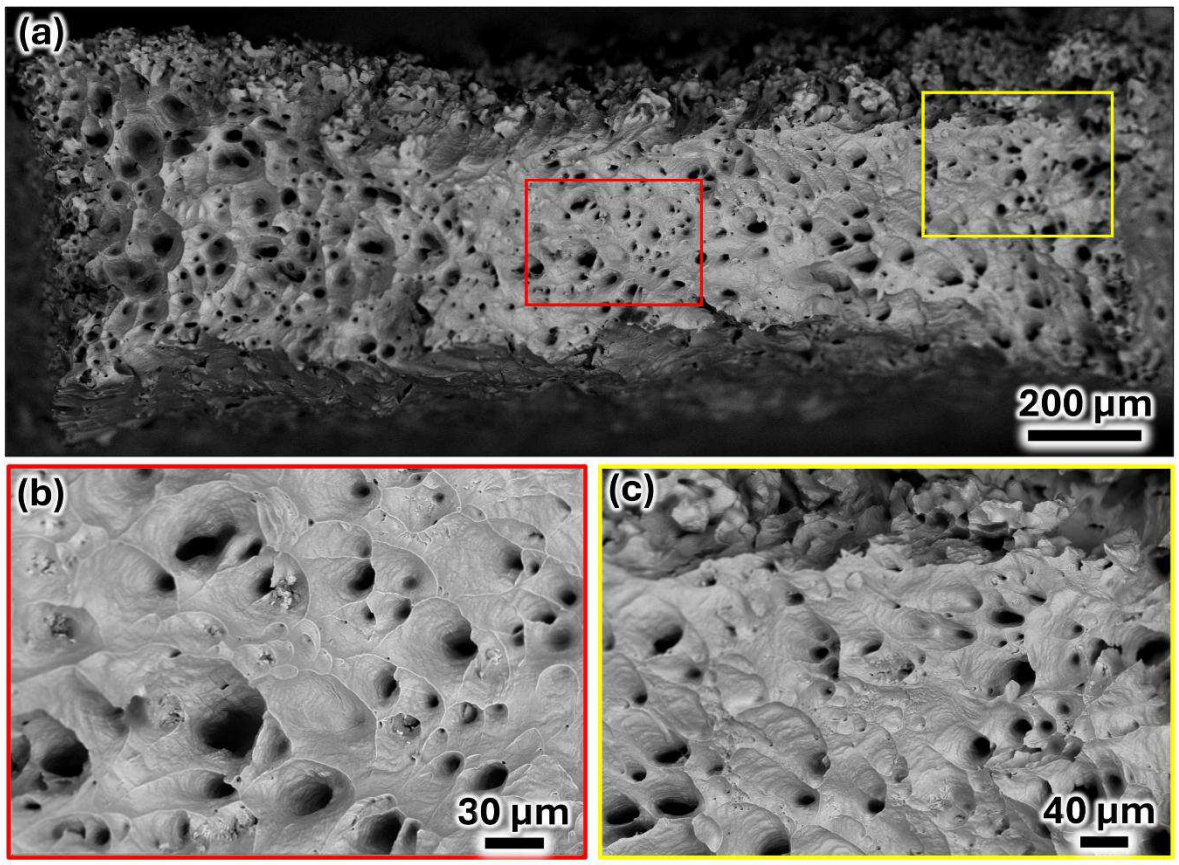


Fig. 9 SEM fractographs of a binder-jetted SS316L tensile specimen fractured without hydrogen charging. (a) Overview of the fracture surface. (b) Higher-magnification view of the region framed in red in (a). (c) Higher-magnification view of the region framed in yellow in (a). The surface is covered by dimples of varying size, some containing residual inclusions, which is characteristic of ductile microvoid coalescence.

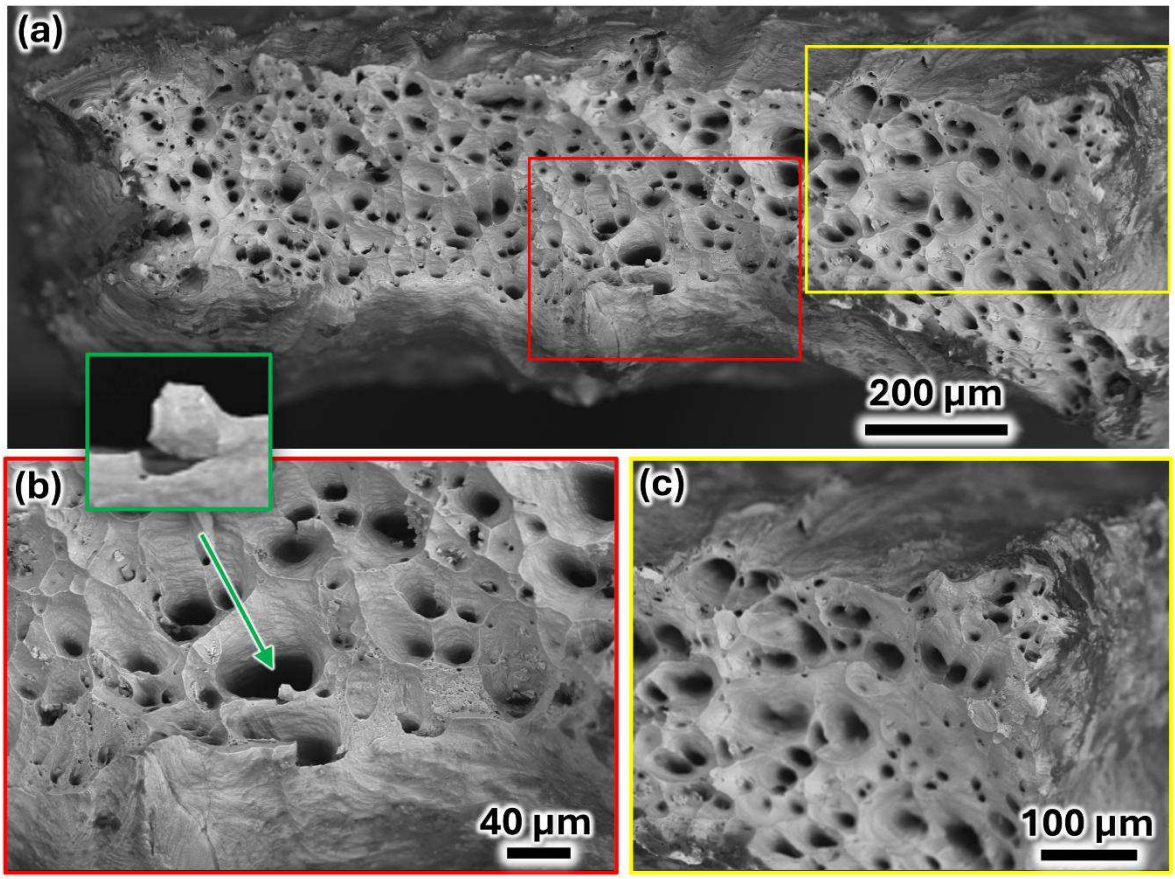


Fig. 10 SEM fractographs of a binder-jetted SS316L tensile specimen fractured after electrochemical hydrogen charging (0.1 M NaCl, 50 °C, −10 mA/cm², 7 d). (a) Overview of the fracture surface. (b) Higher-magnification view of the region framed in red in (a). The inset framed in green shows a magnified view of the site indicated by the green arrow, where a tiny crack was found; such cracks occurred at only a few sites, possibly at grain boundaries or microvoid peripheries. (c) Higher-magnification view of the region framed in yellow in (a). Apart from these isolated cracks, the surface shows the same dimpled, ductile microvoid-coalescence morphology as the uncharged specimen in Fig. 9.

4 Discussion

Vacuum sintering produced the intended austenitic grain structure. The coarse equiaxed austenite grains with annealing twins offer few barriers to dislocation motion, which most likely explains the soft and highly ductile behavior.

Austenite exhibits high hydrogen solubility and low hydrogen diffusivity [38]. Fick's law calculations therefore show that electrochemical charging at 50 °C concentrates hydrogen in a thin surface layer of about 77 µm, while the core of the gauge section remains hydrogen-free. The same calculation gives a penetration depth of about 4.4 mm for gaseous charging at 850 °C. This exceeds the specimen half-thickness of ~0.5 mm and distributes hydrogen through the full cross-section. Both charging routes nevertheless leave the strength and ductility unchanged.

Three possible factors explain this resistance to hydrogen embrittlement. First, austenite is in general a stable phase with low susceptibility to hydrogen embrittlement [38]. Second, the susceptibility to hydrogen embrittlement increases with strength [39]. In ferritic steels, the susceptibility rises steeply above yield strengths of about 400–500 MPa [40] . We therefore assume that the alloy lies in a strength range of low susceptibility. The low strength may also limit embrittlement via strain-induced α′-martensite. In metastable austenitic steels, this martensite promotes hydrogen embrittlement by providing fast diffusion paths and a hydrogen-susceptible phase [41]. At yield strengths well below this range for ferritic steels, this path contributes little to embrittlement.

Third, observations suggest that oxide inclusions formed during the printing process act as hydrogen traps at their interfaces with the austenite matrix [42]. Hydrogen bound at these interfaces remains immobile during tensile loading. The amount of diffusible hydrogen available to reach slip bands and void nuclei is therefore reduced. The micrographs support this interpretation. Gaseous charging at 850 °C leaves the grain structure, the annealing twins and the distribution of cavities unchanged. The charged and uncharged specimens therefore share the same starting microstructure. The inclusions fall out during polishing, which shows weak bonding between the inclusions and the matrix. During straining, these weak interfaces decohere and nucleate voids. The voids and pores elongate along the loading axis, grow during necking and coalesce into larger cavities near the fracture surface. Both conditions show the same dense slip bands, elongated cavities, necking and inclined fracture surface. Both, therefore, fail by ductile microvoid coalescence, and hydrogen leaves the deformation and fracture mechanisms unchanged.

The fractographs support this interpretation. Both the uncharged and the electrochemically charged specimen fractured by ductile microvoid coalescence (Fig. 9, Fig. 10), in line with the unchanged stress–strain response (Fig. 6, Table 3). No extended brittle regions were found after charging. The tiny cracks at a few microvoid rims on the charged specimen (Fig 10b) are the only sign of possible hydrogen-assisted damage. Such sites are plausible, because inclusion interfaces and grain boundaries trap hydrogen, and the local hydrogen concentration there may exceed the average and weaken the interface. The cracks were isolated, however, and neither linked up nor changed the fracture mode. Electrochemical charging at 50 °C also confines hydrogen to a surface layer of about 77 µm, while the rest of the gauge section remains hydrogen-free and carries the load. Damage that is confined to this layer and limited to a few sites would therefore not noticeably change the stress–strain response. Because the cracks are so few, and the SEM images cannot show whether they follow grain boundaries or microvoid rims, they indicate a possible but minor hydrogen effect rather than a change in the failure mechanism.

5 Conclusions

- Vacuum sintering at 1370 °C produced miniature BJT SS316L tensile specimens with a mean relative density of 98 ± 1%. Increasing the sintering dwell from 90 to 180 min did not appreciably change density but improved strength and reduced ductility.
- Neither electrochemical hydrogen charging nor gaseous hydrogen charging caused a change in the stress–strain behavior, suggesting no evident susceptibility to hydrogen embrittlement.
- The sintered microstructure consists of equiaxed austenite grains of 100–150 µm with annealing twins, residual pores and oxide inclusions. Gaseous hydrogen charging leaves this microstructure unchanged, and both charged and uncharged specimens fail by ductile microvoid coalescence; SEM fractography of the uncharged and electrochemically charged specimens shows dimpled fracture surfaces, with tiny cracks at only a few microvoid rims in the charged specimen.
- The stable austenitic matrix and the low yield strength limit embrittlement, and oxide inclusions probably trap hydrogen at their interfaces. Binder-jetted SS316L is therefore a promising candidate for hydrogen-exposed applications.

References

1. Chen M, Liu X, Wang Y, et al (2026) Challenges, Solutions, and Future Perspectives in Metal Additive Manufacturing: A Review. J Mater Eng Perform 35:21649–21680. https://doi.org/10.1007/s11665-02
2. Wei S, Cai Y, Wang Q, Kong J (2026) Research Progress and Prospect of Laser Additive Manufacturing of Ultra-High-Strength Steel. Journal of Materials Engineering and Performance 2025 35:15 35:14285–14316. https://doi.org/10.1007/S11665-025-12334-8
3. Srivastava M, Jayakumar V, Udayan Y, et al (2024) Additive manufacturing of Titanium alloy for aerospace applications: Insights into the process, microstructure, and mechanical properties. Appl Mater Today 41:102481. https://doi.org/10.1016/J.APMT.2024.102481
4. Cunningham CR, Flynn JM, Shokrani A, et al (2018) Invited review article: Strategies and processes for high quality wire arc additive manufacturing. Addit Manuf 22:672–686. https://doi.org/10.1016/J.ADDMA.2018.06.020
5. Javidrad H, Koc B, Bayraktar H, et al (2024) Fatigue performance of metal additive manufacturing: a comprehensive overview. Virtual Phys Prototyp 19:. https://doi.org/10.1080/17452759.2024.2302556
6. Jiang X, Lu J, Zhao N, et al (2024) A Review of Wear in Additive Manufacturing: Wear Mechanism, Materials, and Process. Lubricants 12:321. https://doi.org/10.3390/LUBRICANTS12090321
7. Kotadia HR, Gibbons G, Das A, Howes PD (2021) A review of Laser Powder Bed Fusion Additive Manufacturing of aluminium alloys: Microstructure and properties. Addit Manuf 46:102155. https://doi.org/10.1016/J.ADDMA.2021.102155
8. Narra SP, Rollett AD, Ngo A, et al (2023) Process qualification of laser powder bed fusion based on processing-defect structure-fatigue properties in Ti-6Al-4V. J Mater Process Technol 311:117775. https://doi.org/10.1016/J.JMATPROTEC.2022.117775
9. Liu H, Yu H, Guo C, et al (2024) Review on Fatigue of Additive Manufactured Metallic Alloys: Microstructure, Performance, Enhancement, and Assessment Methods. Advanced Materials 36:2306570. https://doi.org/https://doi.org/10.1002/adma.202306570DigitalObjectIdentifier(DOI)
10. Gruber K, Szymczyk-Ziółkowska P, Dziuba S, et al (2023) Fatigue crack growth characterization of Inconel 718 after additive manufacturing by laser powder bed fusion and heat treatment. Int J Fatigue 166:107287. https://doi.org/10.1016/J.IJFATIGUE.2022.107287
11. Avanzini A (2023) Fatigue Behavior of Additively Manufactured Stainless Steel 316L. Materials 16:. https://doi.org/10.3390/ma16010065
12. Kumar P, Jayaraj R, Suryawanshi J, et al (2020) Fatigue strength of additively manufactured 316L austenitic stainless steel. Acta Mater 199:225–239. https://doi.org/10.1016/j.actamat.2020.08.033
13. Berez J, Saldana C (2021) Fatigue of laser powder bed fusion processed 17-4 stainless steel using prior process exposed powder feedstock. J Manuf Process 71:515–527. https://doi.org/10.1016/J.JMAPRO.2021.09.045
14. Hemmasian Ettefagh A, Guo S, Raush J (2021) Corrosion performance of additively manufactured stainless steel parts: A review. Addit Manuf 37:101689. https://doi.org/10.1016/J.ADDMA.2020.101689
15. Yu H, Zhao Q, Fu J, et al (2025) The design of oxidation resistant Ni superalloys for additive manufacturing. Addit Manuf 97:104616. https://doi.org/10.1016/J.ADDMA.2024.104616
16. Oros TJ, Son K, Hodge AM, Kassner ME (2024) The high temperature creep and fracture behavior of Inconel 718 produced by additive manufacturing. Scr Mater 251:116208. https://doi.org/10.1016/J.SCRIPTAMAT.2024.116208
17. Wang J, Li Z, Wu Q, Xu T (2025) The creep properties and mechanism of Ti-6Al-4V with ultra-low β contents fabricated by wire arc additive manufacturing. Additive Manufacturing Frontiers 4:200246. https://doi.org/10.1016/J.AMF.2025.200246
18. Lin J, Chen F, Liu F, et al (2020) Hydrogen permeation behavior and hydrogen-induced defects in 316L stainless steels manufactured by additive manufacturing. Mater Chem Phys 250:. https://doi.org/10.1016/j.matchemphys.2020.123038
19. Singer L, Harris ZD, Burns JT, Scully JR (2025) The role of hydrogen-metal interactions in hydrogen environmentally assisted cracking susceptibility in additively manufactured 17-4 PH stainless steel. Materials Science and Engineering: A 927:. https://doi.org/10.1016/j.msea.2025.147996
20. Endrös P, Deconinck L, Razavi N, et al (2025) Hydrogen embrittlement in Ti–6Al–4V: A comparative review of conventional and additive manufacturing. Int J Hydrogen Energy 179:. https://doi.org/10.1016/j.ijhydene.2025.151710
21. Santos Maldonado CT, Zafra A, Martínez Pañeda E, et al (2024) Influence of dislocation cells on hydrogen embrittlement in wrought and additively manufactured Inconel 718. Commun Mater 5:. https://doi.org/10.1038/s43246-024-00654-6

22. Feng J, Zhang X, Chu Y, Wan J (2024) Hydrogen Embrittlement of Ni-Based Superalloy Inconel 625 Fabricated by Wire Arc Additive Manufacturing: The Role of Laves Phase. Metals and Materials International 30:872–885. https://doi.org/10.1007/s12540-023-01546-z
23. Behvar A, Khorasani MB, Mohajerani S, et al (2026) Hydrogen embrittlement of additively manufactured NiTi shape memory alloys: Review on interactions between microstructure and mechanical properties. Prog. Mater. Sci. 159
24. Nabizada A, Moallemi M, Javaheri V, et al (2026) Hydrogen embrittlement evaluation of wire arc additive manufactured 316L stainless steel: Evidence of hydrogen induced hardening, enhanced decohesion, and assisted localized deformation. Addit Manuf 124:. https://doi.org/10.1016/j.addma.2026.105237
25. Efremenko B, Chabak Y, Falat L, et al (2026) Hydrogen-Induced Effects on Tensile Properties and Impact Toughness in Additively Manufactured vs. Wrought Austenitic Stainless Steels. Corrosion and Materials Degradation 7:14. https://doi.org/10.3390/cmd7010014
26. Álvarez G, Harris Z, Wada K, et al (2023) Hydrogen embrittlement susceptibility of additively manufactured 316L stainless steel: Influence of post-processing, printing direction, temperature and pre-straining. Addit Manuf 78:. https://doi.org/10.1016/j.addma.2023.103834
27. Gamboa G, Babakr A, Young ML (2025) Effect of Hydrogen and Hydrogen-Blended Natural Gas on Additive-Manufactured 316L Stainless Steel in Ambient Oil and Gas Environments. Metals (Basel) 15:. https://doi.org/10.3390/met15070689
28. Kong D, Dong C, Ni X, et al (2020) Superior resistance to hydrogen damage for selective laser melted 316L stainless steel in a proton exchange membrane fuel cell environment. Corros Sci 166:. https://doi.org/10.1016/j.corsci.2019.108425
29. Claeys L, Deconinck L, Verbeken K, Depover T (2023) Effect of additive manufacturing and subsequent heat and/or surface treatment on the hydrogen embrittlement sensitivity of 316L austenitic stainless steel. Int J Hydrogen Energy 48:36142–36157. https://doi.org/10.1016/j.ijhydene.2023.05.215
30. Yang S, Juan R, Lian J (2026) Towards sustainable hydrogen infrastructures: Additive manufacturing of metallic materials for enhanced resistance to hydrogen embrittlement. Materials Today Sustainability 34:. https://doi.org/10.1016/j.mtsust.2026.101339
31. Sachs EM, Haggerty JS, Cima MJ, Williams PA (1993) Three-dimensional printing techniques
32. Munsch M, Schmidt-Lehr M, Wycisk E (2018) Metal Additive Manufacturing with sinter-based technologies
33. (2011) ISO 3953:2011 - Metallic powders — Determination of tap density. https://www.iso.org/standard/56508.html. Accessed 29 Jun 2025
34. (1981) ISO 3923-2:1981 - Metallic powders — Determination of apparent density — Part 2: Scott volumeter method
35. (1985) BS 5600-2.6:1985 Powder metallurgical materials and products. Methods
36. (1977) ISO 4324:1977 - Surface active agents — Powders and granules — Measurement of the angle of repose
37. (2017) Test Methods for Density of Compacted or Sintered Powder Metallurgy (PM) Products Using Archimedes Principle. ASTM International, West Conshohocken, PA
38. Grant DM, Cummings DL, Blackburn DA (1988) Hydrogen in 316 steel — diffusion, permeation and surface reaction. Journal of Nuclear Materials 152:139–145. https://doi.org/10.1016/0022-3115(88)90319-4
39. Gangloff RP (2003) Hydrogen-assisted Cracking. Comprehensive Structural Integrity 6:31–101. https://doi.org/10.1016/B0-08-043749-4/06134-6
40. Nanninga N, Slifka A, Levy Y, White C (2010) A Review of Fatigue Crack Growth for Pipeline Steels Exposed to Hydrogen. J Res Natl Inst Stand Technol 115:437. https://doi.org/10.6028/JRES.115.030
41. Tsong-Pyng P, Altstetter CJ (1986) Effects of deformation on hydrogen permeation in austenitic stainless steels. Acta Metallurgica 34:1771–1781. https://doi.org/10.1016/0001-6160(86)90123-9
42. Pressouyre GM (1979) A classification of hydrogen traps in steel. Metallurgical Transactions A 10:1571–1573. https://doi.org/10.1007/BF02812023

Statements and Declarations

Funding
The authors did not receive support from any organization for the submitted work.

Competing Interests
The authors declare no competing interests.

Author Contributions
Emrecan Soylemez coordinated the study, organized and conducted the printing and sintering experiments, and wrote the first draft and subsequent revisions. Cem Örnek organized the characterization, hydrogen exposure, and tensile testing; analyzed and interpreted the results; and contributed to writing and revising the manuscript. Burçak Avcı conducted the characterization, hydrogen exposure, and tensile testing and revised the manuscript.

Acknowledgments

The authors would like to thank Mehmet Fatih Yalcin, Zeki Aslan, Ali Cem Çetin, and Ali Emre Ozanlayan at Istanbul Technical University for their assistance with characterization and experimental studies.